

# Magnetic Case Study: Raglan Mine

Laura Davis

May 24, 2006

## Research Objectives

The objective of this study was to test the tools available in **EMIGMA** (PetRos Eikon) for their utility in analyzing magnetic data in terms of the usefulness and efficiency of available algorithms and the ease of using the interface. Many different types of tools were used together to get a clear understanding of the geophysics of the problem, and what the geophysics means for the structure of the subsurface. For the purpose of this testing, field data from a portion of the Raglan Mine site was examined.

## Introduction

Raglan Mine is a nickel and copper mine owned by Falconbridge. It is located in northern Quebec at a latitude of  $61^{\circ}39'N$  and a longitude of  $73^{\circ}41' W$ . The goal was to create a model of the subsurface for part of the Raglan Mine site using magnetic data collected in the region. The approach was to create models in **EMIGMA** and run forward simulations. The synthetic data was compared with the field data in 3-D plots, contour plots, and plots along each survey line, and the model was further refined. Derivatives and upward continuation were used to assist with the development of improved models. To help constrain depths and to provide information on structure, Euler solutions were found for the data, and further models were produced. Susceptibility inversion was performed to obtain further information on the distribution of magnetic material in the subsurface.

## Magnetic Data

### *Data Collection*

The magnetic data used for this study were obtained in the mid-1990's. The data were collected on a grid between 97 300 m and 99 300 m east (x-direction) and 36 000 m and 37 000 m north (y-direction). The survey lines run north-south and are spaced at intervals of 100 m and the distance between data points along a survey line is 12.6 m on average. Data was not collected in the southwest corner and along part of line 97 600 due to lakes. **Figure 1** shows the profile lines and the data points.

### *Background Field*

Based on the location of the mine and the approximate time of the survey, the IGRF was calculated to have an inclination of  $82^{\circ}$ , a declination of  $-32^{\circ}$  and an intensity of 58 786 nT. The background field calculated from the data is 58 157 nT, and this is the value that was used for the modeling. Based on the contour plot and the plots along the survey lines, the background level appears to be slightly higher between lines 97 500 and 97 800. This is assumed to be the result of a leveling error during the data collection. It was not corrected.

### *Anomalies*

Two significant anomalies and several small anomalies can be observed in the interpolated data in **Figure 2**. The first is observed in the southern half of the grid area between lines 97 600 and 99 100 with an overall trend of about  $105^{\circ}$ . It is a positive anomaly with small, negative anomalies on either side. The amplitude of the anomaly varies substantially across the region, with a maximum amplitude of about 3000 nT. Due to the width, length, and size of the anomaly, it is assumed to be caused by a linear feature with induced magnetization. The second is a localized anomaly in the center of the

northern half of the grid that is 4000nT below the background level, with smaller positive anomalies on either side. Due to the amplitude and size of the anomaly, it is assumed to be caused by a small body with remnant (i.e. permanent) magnetization.

## Forward Modeling

### *Development of Models*

Using the magnetic data, the location and susceptibility of bodies that could lead to magnetic anomalies were guessed and a model of the subsurface was created in **EMIGMA**. The models were constructed by inserting prisms and adjusting their properties (orientation, size, and susceptibility). Following the creation of a possible model, a forward simulation was run to obtain synthetic magnetic data. The amplitude, width and location of the anomalies in the real and synthetic data were compared. The properties of the anomalous bodies in the model were adjusted so that the synthetic data would match the field data more closely.

Several algorithms and interactions are available for forward simulation. For Born (weak scattering) methods, it is assumed that the induced magnetization is parallel to the background field; this assumption is not made for LN (localized non-linear) scattering. Superposition under LN scatter was generally used for forward simulation, but Born (analytic method) and Born (numerical method) were also performed and compared with superposition under LN scattering for the two models. All three methods were very quick, making it easy to test the models, but the results of the different methods were not identical. (See Figure 3.) The fact that the LN and Born methods do not produce the same results suggests that weak scattering is not the best approximation for the model, although the difference between the synthetic data for superposition under LN scattering and Born (numerical method) was quite small (no more than 60 nT). No difference between these two could be detected on most profile plots. In fact, the difference between the Born (analytic method) and Born (numerical method) was much larger. The difference in intensity (up to 350 nT) was apparent on most survey lines, and a difference in the shape of the anomalies in the synthetic data was sometimes apparent.

The long anomaly in the southern half of the survey area varies in trend, amplitude and width across the region. Several small bodies (possibly dykes) with different properties are needed to capture the variation of this anomaly. The asymmetrical shape of this anomaly in profile plots suggests that these bodies are dipping. The dip direction appears to be to the north in general, but possibly to the south in some places. The synthetic data matches the field data best in width and amplitude when the bodies are thin and relatively shallow. The anomaly is assumed to be caused only by induced magnetization.

The other significant anomaly was isolated and modeled in a separate survey. Since the anomaly appears to be directly opposite the ambient field, an inclination of  $-80^{\circ}$  and a susceptibility of 0 were assumed. The amplitude and extent of the positive peaks on either side of the large negative anomaly could not be obtained by a model containing only one body with remnant magnetization. Small, thin bodies with induced magnetization were placed on either side of the remnant body to match the magnetic data more closely.

### *Results from Forward Simulation*

The initial phase of forward modeling succeeded in obtaining a reasonably good model of the remnant body and of the western part of the larger anomaly. A 3-D plot of Model 1 is shown in **Figure 4**, and plots of the synthetic and real data along survey lines are shown in **Figure 5**.

The amplitude and the location of the large anomaly were captured fairly well in the synthetic data; however, the positive anomaly that is observed to the south of the large anomaly in the field data is too small in the synthetic data, and the overall anomaly is too continuous on the contour plot. As well, the amplitude of the anomaly in the eastern half of the survey in the synthetic data did not match the actual data well. The anomaly caused by the remnant body is captured well in the model, as shown in **Figure 5b**.

## **Interpolation and Derivatives**

The magnetic data was interpolated using both 32 x 128 and 64 x 256 grids. The derivatives were calculated by transforming the data into the frequency domain using the FFT (Fast Fourier Transform). The FFT is an algorithm that allows the discrete Fourier transform to be computed more quickly by breaking it down into smaller Fourier transforms, and requires the grid to be in powers of 2. Once in the frequency domain, the derivatives for the data can be calculated more easily. The derivatives in the x, y, and z directions were observed in Emigma. A plot of the derivatives in the north-south direction is shown in **Figure 6**.

Laplace's equation allows the magnetic potential to be found at any height for a given x and y. Upward continuation was performed on the interpolated data for heights of 30 m, 100 m, 300 m, and 500 m to obtain information on the regional structure. Few of the small anomalies remain at 100 m. The regional structure is apparent at 300m, as shown in **Figure 7**. There is a large structure trending approximately east-west in the vicinity of the large anomaly with a greater intensity to the west. There is also a large structure with a negative anomaly near the remnant body. A north-south trending structure is observed on the west of the plot; however, this is probably due to the leveling error.

## **Euler Solutions**

Euler solutions were obtained using Emigma to provide information on the depth of the anomalies. A 64 x 256 derivative grid was preferable to a 32 x 128 derivative grid because it provides significantly more solutions. The size of the window affects the type of solutions that can be found. The maximum depth for solutions is about twice the window size (Reid, 1990). As well, large windows may cause problems because anomalies from different sources may occupy the same window, and small anomalies may cause problems because large anomalies are poorly depicted in a small window (Reid, 1990). Solutions were found for a variety of window sizes between 24 and 120 rows, and 4 and 17 columns. A window of 50 rows by 8 columns (giving a height of 213 m and a width of 227 m), a transverse moving step of 12 rows and an inline moving step of 2 columns worked well for this data set.

Post-processing (deviation error removal, uncorrelated solution removal and clustering ) was then used to remove poorly-constrained and poorly-clustered solutions. Since the largest deviations were 21 cm, little deviation error removal was needed. A deviation error removal of 15%, and an uncorrelated solution removal of 35% and a minimum cluster size of 10 m were found to remove nearly all solutions that are probably not related to structure and to retain enough solutions to mark the outlines of the anomalies. Clustering with a distance of 10 m between bodies was used to group solutions. The processed Euler solutions are shown in **Figure 8**. For this data set, which is relatively small, the calculation of the Euler solutions and the post-processing were quick, but it took some time to figure out the appropriate settings. The process was repeated numerous times with different windows sizes, moving steps, and post-processing settings.

The majority of the solutions are located near the two anomalies mentioned above. Most of the solutions for the remnant body are less than 80 m deep and most of the solutions for the larger anomalous body were less than 100 m deep. This suggests that the bodies causing the magnetic anomalies are relatively shallow. Solutions were obtained for structural indices between 0.5 and 3.5, and slightly more solutions were observed for indices between 0.5 and 2.

## **Additional Forward Modeling**

The Euler solutions, as well as the upward continuation and derivative plots, were used to further refine the model of the subsurface, particularly the depths and the dips of the anomalous bodies. Shallower dips were used to improve the match for the shape of the anomalies in certain areas. Consistent dips across the region were also used because it is likely that the structures having similar strikes were formed as the result of similar processes, and probably have approximately the same dip.

Contour plots were also used to obtain more control on the location of the bodies causing the large anomaly. The contour plot (see **Figure 2**), which is discontinuous in terms of the size and the trend of the anomaly, suggests that there are six bodies with slightly different strikes that are causing the anomaly.

## **Final Model from Forward Simulation**

### *Structure of the Subsurface in the Final Model*

**Figure 9** is a visualization of the model. Six bodies dipping at about  $30^\circ$  N with strikes varying between  $268^\circ$  and  $288^\circ$ , and susceptibilities between 0.03 and 0.18 create the large anomaly. The eastern-most body extends very deep and has a low susceptibility. The body with remnant magnetization has an inclination of  $-80^\circ$  and a RM of 0.25. There are two bodies surrounding the remnant body with induced magnetization that have dips of  $-30^\circ$  N and susceptibilities of 0.065 and 0.125. Three smaller bodies with susceptibilities between 0.02 and 0.07 create smaller anomalies.

### *Geological Interpretation*

The main features in the model are a series of linear features that have similar orientations but different magnetic properties. These linear features are the source of the induced magnetization causing the large anomaly in the southern portion of the survey area and the positive anomalies observed near the body with remnant magnetization. A possible explanation is that the area is underlain by a set of small intrusions, possibly dykes. They appear to be very localized intrusions, as the anomalous bodies in the model are not long. Although most of these features do not extend as deeply as would be expected for dykes, this may be because the features are only magnetic near the surface, or depth may not be detected well in the survey. It may be worthwhile to try modeling features that extend much deeper to examine the differences in the synthetic data. The variation in the susceptibilities in the model, which was necessary to capture the change in the amplitude of the anomalies, suggests that these features have different mineral compositions. It is also possible that the magnetic anomaly is caused to some extent by magnetic material that was scraped up during the intrusion, and that the variability in this material caused the change in the amplitude of the anomaly across the region.

### *Results for the Final Model*

The Euler solutions for this model, shown in **Figure 10**, are similar to the Euler solutions for the data. Solutions were found at similar depths for the remnant body and there is a similar distribution of points at different depths, although the model has more Euler solutions between 100 m and 120 m for the

larger anomaly. There are also more Euler solutions near smaller anomalies for the model. The distribution of solutions with the structural index is similar. The overall similarity of the Euler solutions suggests that the general structure and depths are correct.

The contour plots for the model (**Figure 11**) and the data (**Figure 2**) appear similar for major structures. In plots along the profile lines (**Figure 12**), it is noted that the variation in the amplitude of the larger anomaly is captured fairly well in the model; however, the amplitude is both too high and too low for different lines on the eastern part of the anomaly and the shape is does not match well. The size and shape of the anomaly caused by the remnant body is a very good fit. The amplitude of the anomalies due to the surrounding bodies with induced magnetization is good, although the shape is not perfect.

Overall, the synthetic data from the final model fits the field data better than the data from the first model. Part of the difficulty encountered in modeling may have been due to noise in the data. Large fluctuations in magnetic response between adjacent points are noted along certain lines, and the overall trends are not always clear and smooth, as observed along line 98700 in **Figure 12c**.

## Filtering

Filtering was used to smooth out the data because it appears to be quite noisy. Several different types of filtering were tried. Spatial filtering is preferable to digital filtering for the lines with gaps in the data because digital filtering will use points that are very far away from the point of interest in the filtering. The mean and median methods lower the positive peaks substantially; Gaussian filtering is preferable because it weights the points around the central point most heavily. A large deviation smoothes the data too much and a small one produces little modification; it was found that a deviation of 18 m provides a good balance. A large radius uses more points, but this did not make as much of a difference in the results as the deviation. The default, 74.762 m (about 6 points on either side) was generally used. An example of filtered data is shown in **Figure 13**.

## 3-D Susceptibility Inversion

### *Inversion Using the Field Data*

Inversion was used to directly obtain information on the susceptibilities of anomalous bodies that could create the magnetic data. Inversion does not find remnant magnetization, although it can come up with negative susceptibilities.

Matrix inversion was first performed on the data to a depth of 800 m, using both the Born solution (**Figure 14**) and the iterative LN solution. Due to the limited number of cells allowed for matrix inversion, this produced a very coarse model. **Figure 14** is a contour plot of the data from the inverse model using the Born solution.

Optimization inversion was performed using both Model 2 and the model from the matrix inversion as starting points. Inversion was first performed with large cells, and later with small cells to get finer resolution. The coarse inversions were relatively fast, but the finer resolution ones took a few hours. A depth of 800 m and an exponentially spaced grid (base 2) were used in the z direction; however, an exponentially spaced grid was not entirely appropriate because it makes the deep cells very large and the shallow cells very small. Even spacing would not have been ideal either; perhaps an exponentially spaced grid with a base of about 1.5 would have been better. One of the models obtained from

optimization inversion is shown in **Figure 15**, and a contour plot of the data from the inversion is shown in **Figure 16**.

The models obtained from inversion with fine resolution fit the data relatively well (**Figure 17**). However, the amplitude of the remnant body is not large enough (**Figure 17b**) and some of the noise in the data is amplified (**Figure 17c**). Because the background level calculated from the data is not perfect, nearly every cell has a susceptibility above the threshold, which makes the entire model look complex. The sensitivity was set so that a certain susceptibility range could be viewed (see **Figure 15**), but it would have been useful to be able to view susceptibilities with certain absolute values so that points of interest could more easily be determined. In addition, a legend of the colors for the different susceptibilities would also have been useful.

#### *Inversion Using the Filtered Data*

Optimization inversion was performed on the filtered data using the final model as a starting point. Even a coarse inversion fits the filtered data relatively well. Unlike for the field data, the inversion does not excessively amplify the noise when the filtered data is inverted (**Figure 18**).

#### *Interpretation of Inversion Results*

The models from inversion are complex, and it is difficult to discern the strike and dip of the anomalous bodies, probably at least partially due to noisy data (in the case of the inversion of the field data). As well, the inversion does not provide information on the remnant properties, and this is probably why the synthetic data from the inversions matches the field data most poorly near the remnant body. The range of susceptibilities from the inversion is similar to that in Model 2, but the depths are somewhat greater, suggesting that the linear magnetic features in the model should extend somewhat deeper.

## **References**

Reid, A. B. et al. (1990). Magnetic interpretation in three dimensions using Euler deconvolution. *Geophysics*, Vol. 55. 80-91.



### Mag Response Along Line 98200

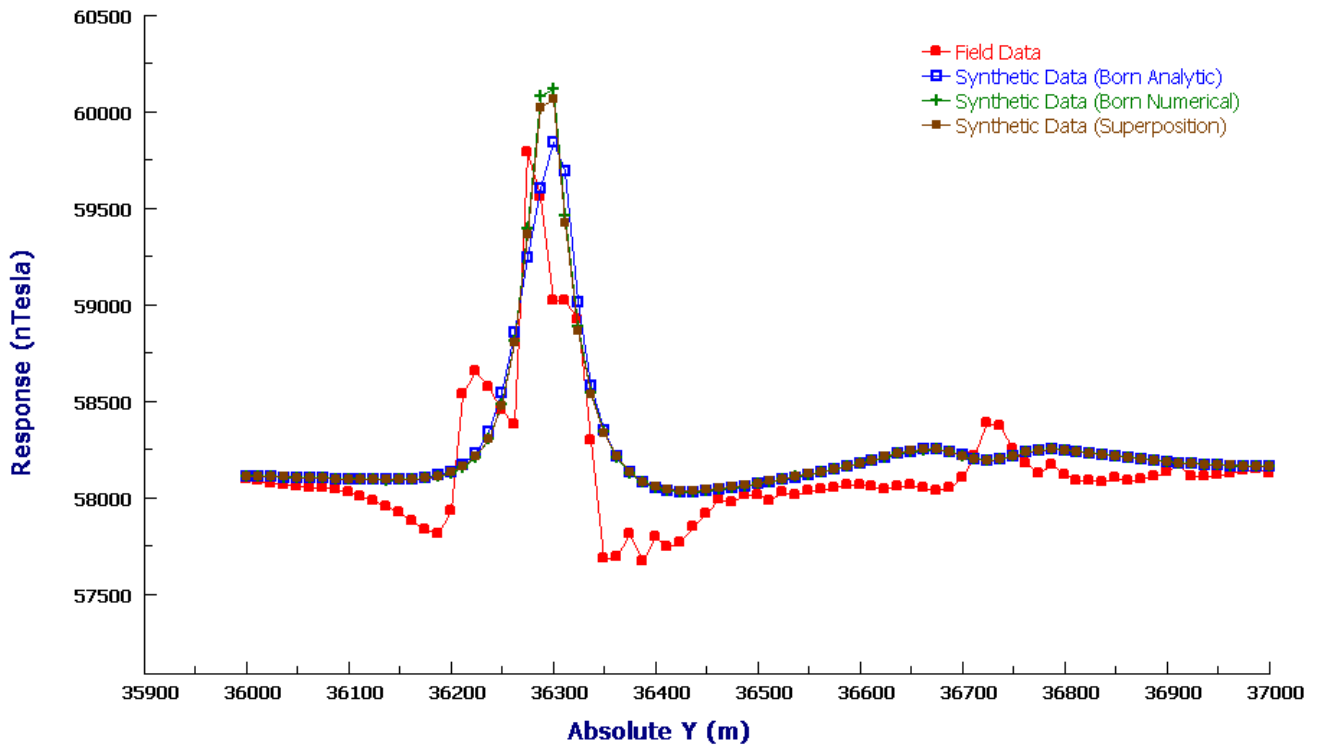


Figure 3: Comparison of the synthetic data obtained for an earlier model using different methods of forward simulation.

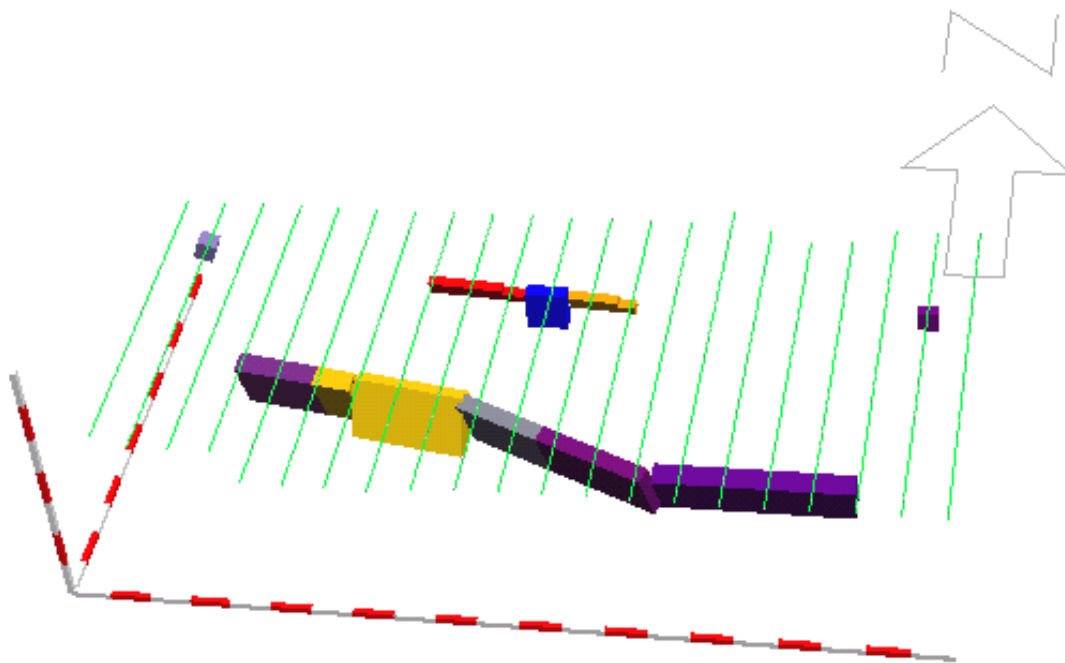


Figure 4: Model 1 from the initial phase of forward modeling.

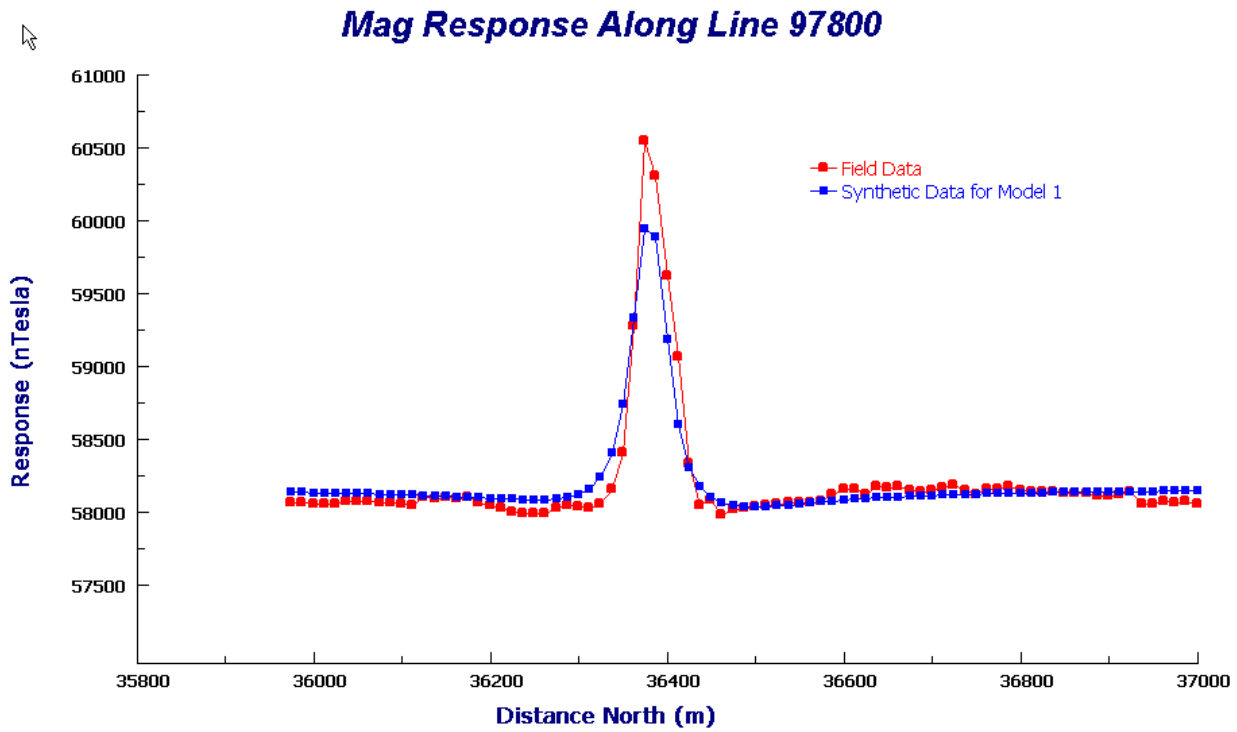


Figure 5a: Comparison of the magnetic response along Line 97800 for the field data and the synthetic data from Model 1.

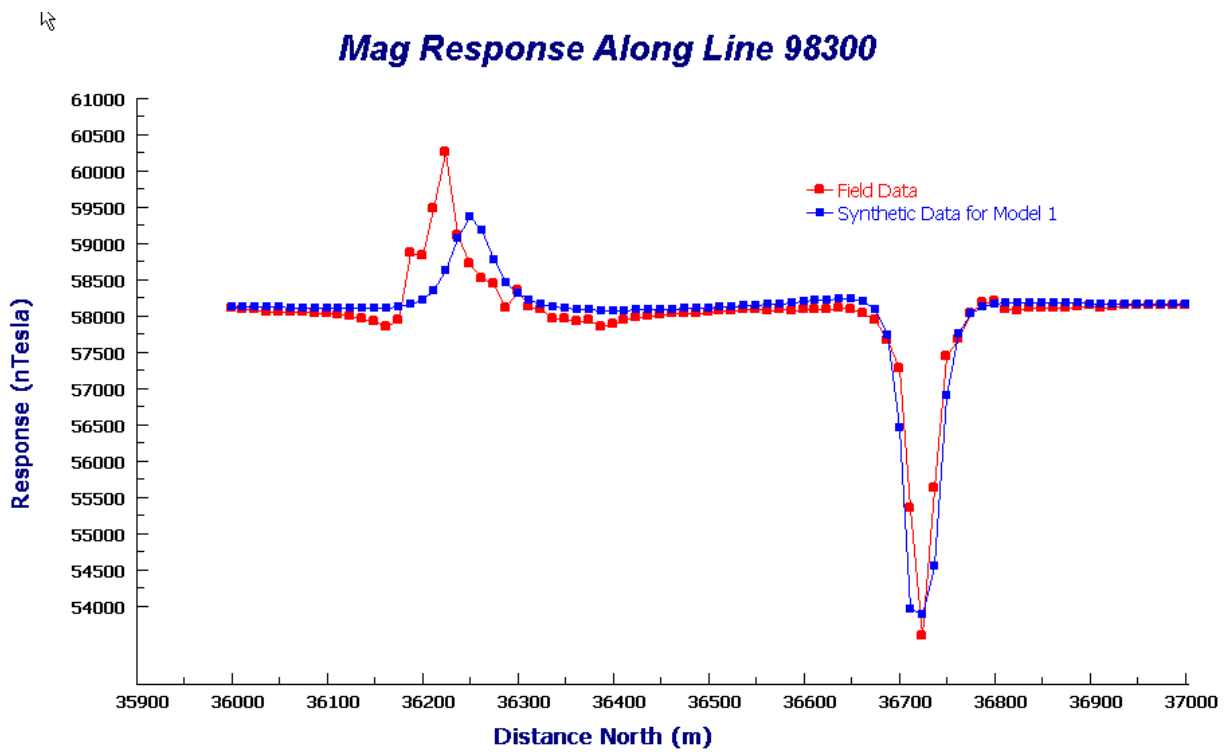


Figure 5b: Comparison of the magnetic response along Line 98300 for the field data and the synthetic data from Model 1.

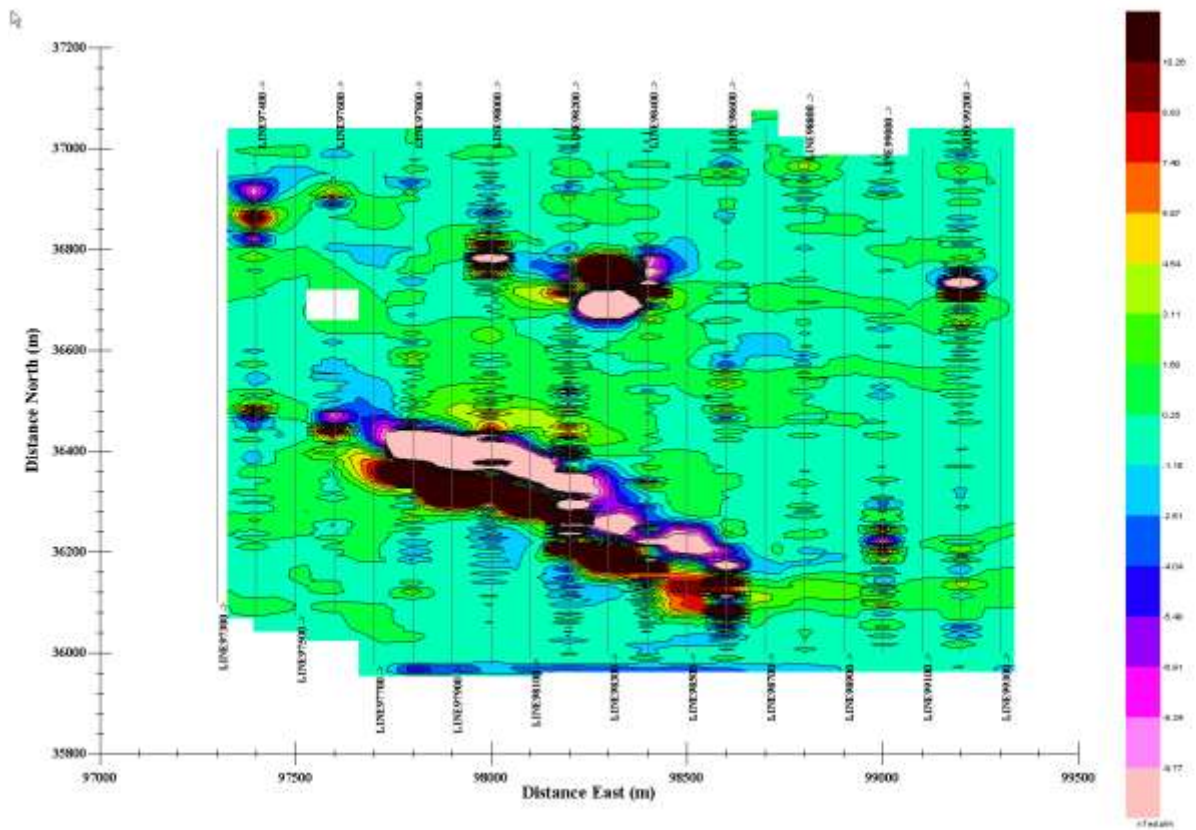


Figure 6: A plot of the derivatives of the magnetic field in the north-south direction. Points that were extrapolated outside a radius of 50 m have been removed.

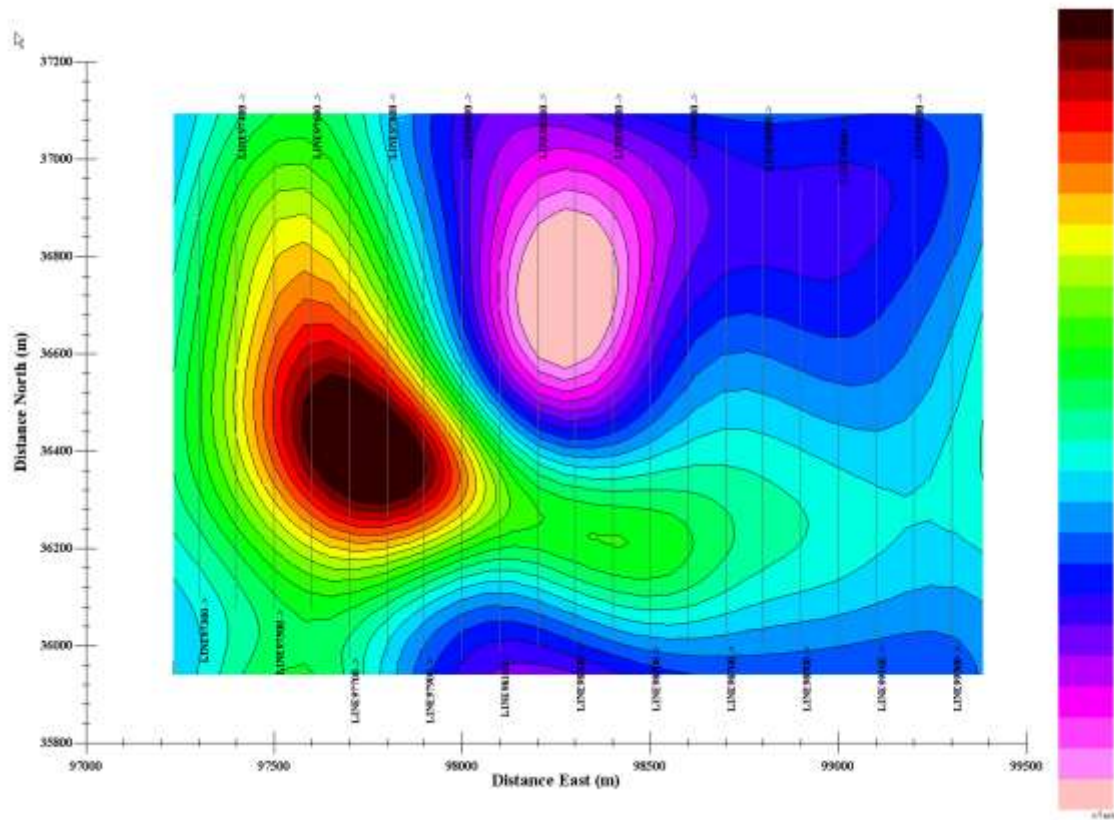


Figure 7: A contour fill of the data after interpolation and upward continuation to a height of 300 m.

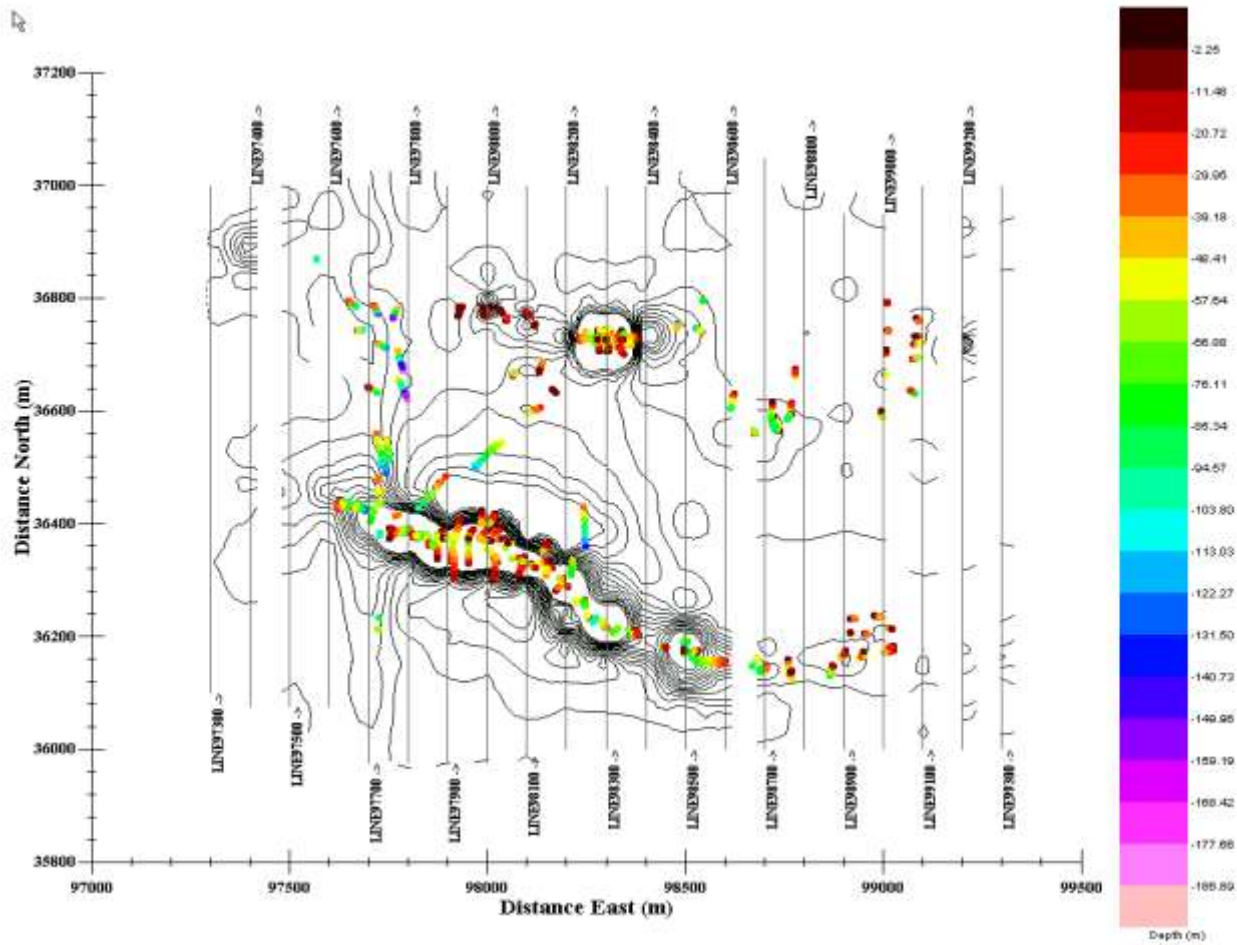


Figure 8: A contour plot of the interpolated data showing the Euler solutions following a deviation error removal of 15%, and an uncorrelated solution removal of 35% with a minimum cluster size of 10 m. A window of 50 rows by 8 columns, a transverse moving step of 12 rows, and an inline moving step of 2 columns were used.

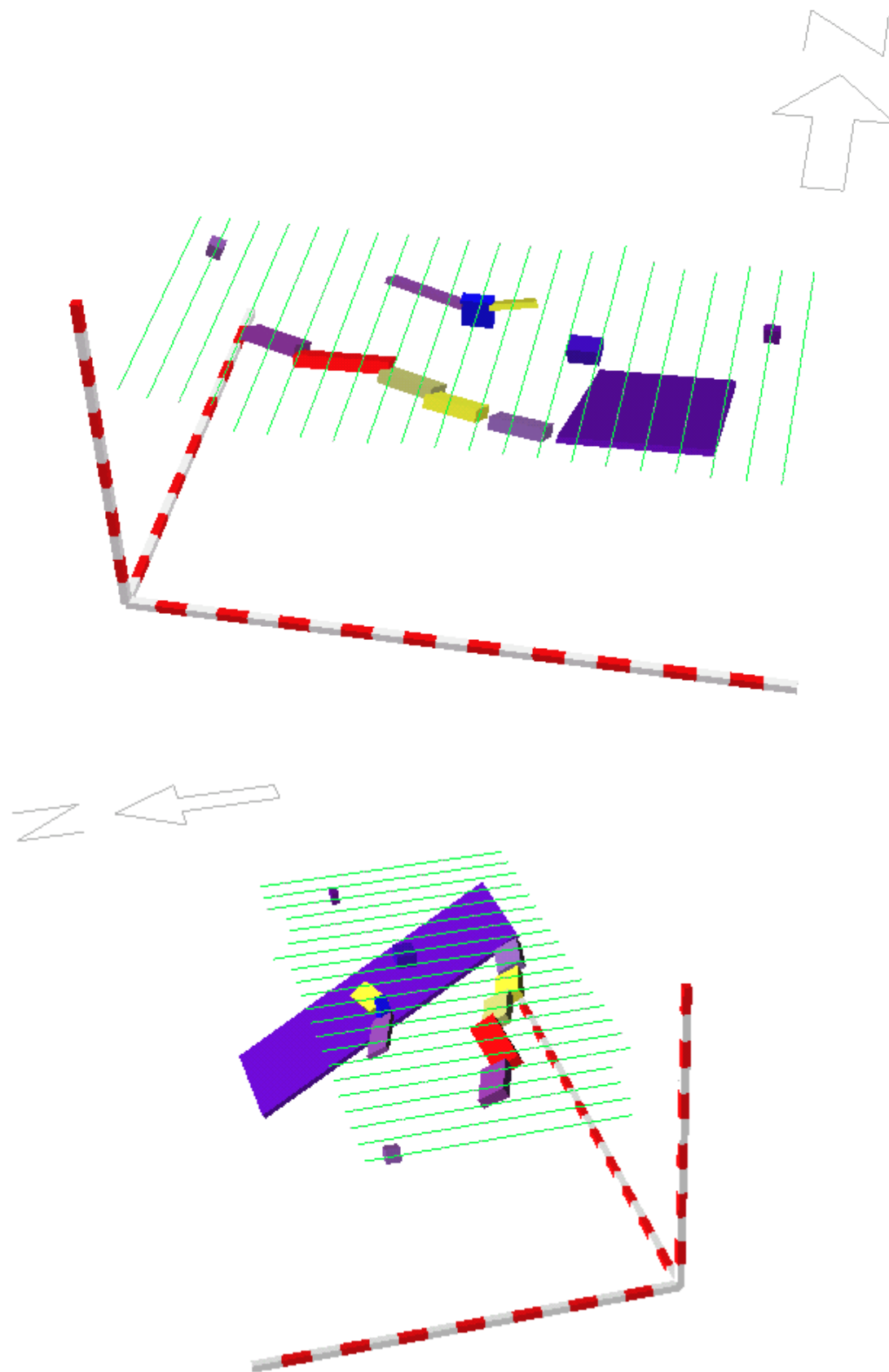


Figure 9: Model 2 from the second phase of forward modeling., shown from two different angles.

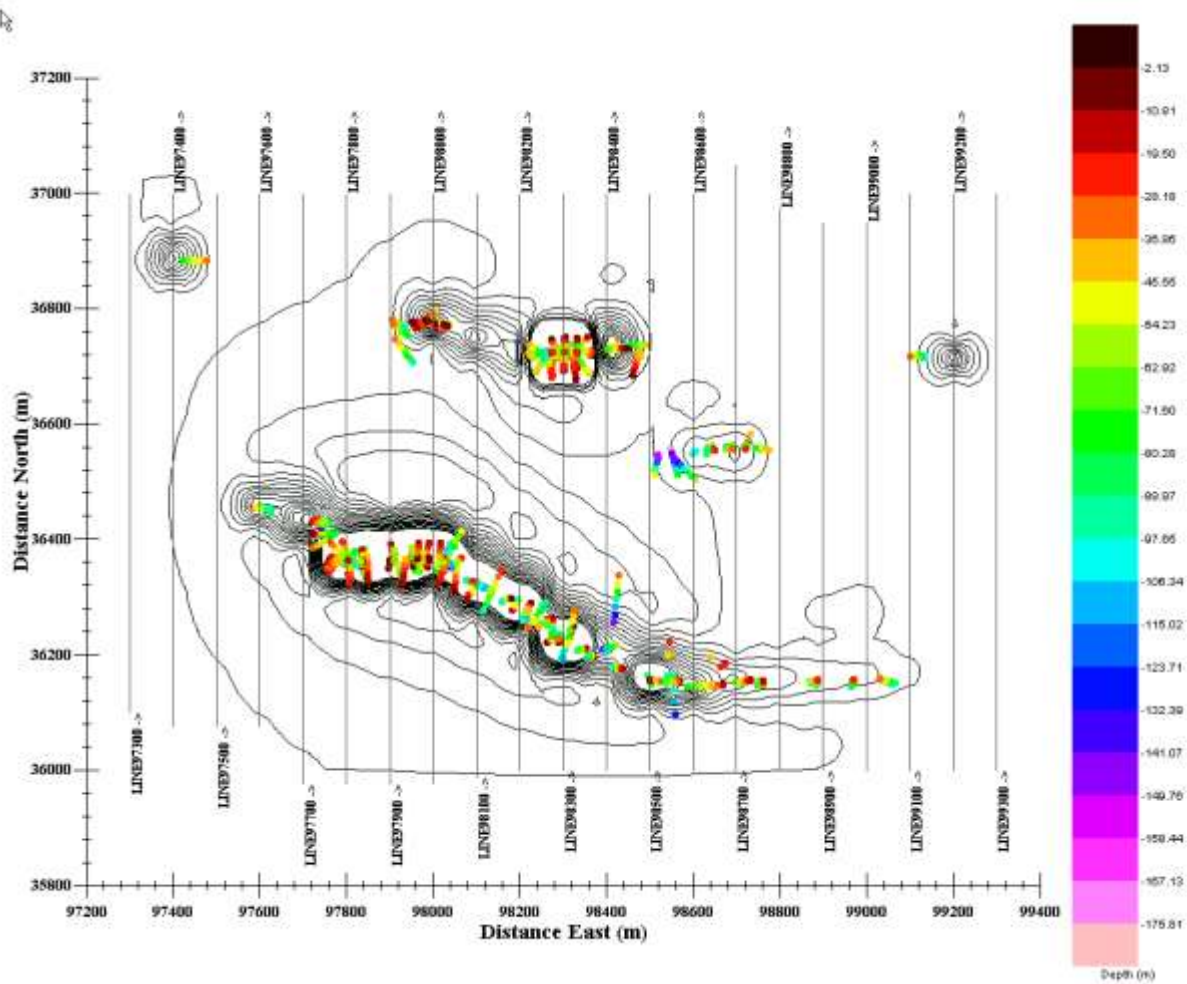


Figure 10: A contour plot of the synthetic data showing the Euler solutions following a deviation error removal of 15%, and an uncorrelated solution removal of 35% with a minimum cluster size of 10 m. A window of 50 rows by 8 columns, a transverse moving step of 12 rows, and an inline moving step of 2 columns were used.

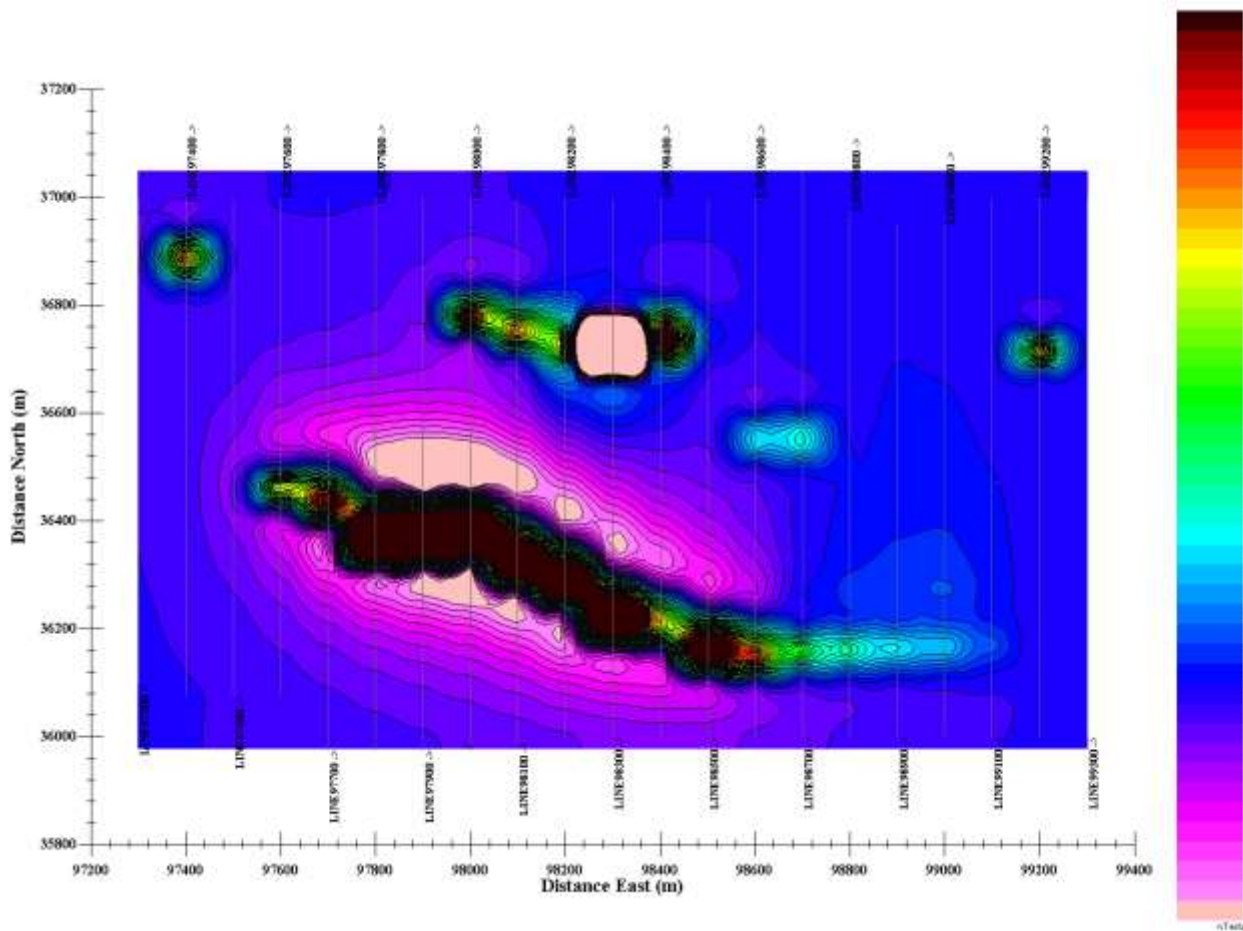


Figure 11: A contour fill of the synthetic data for Model 2.

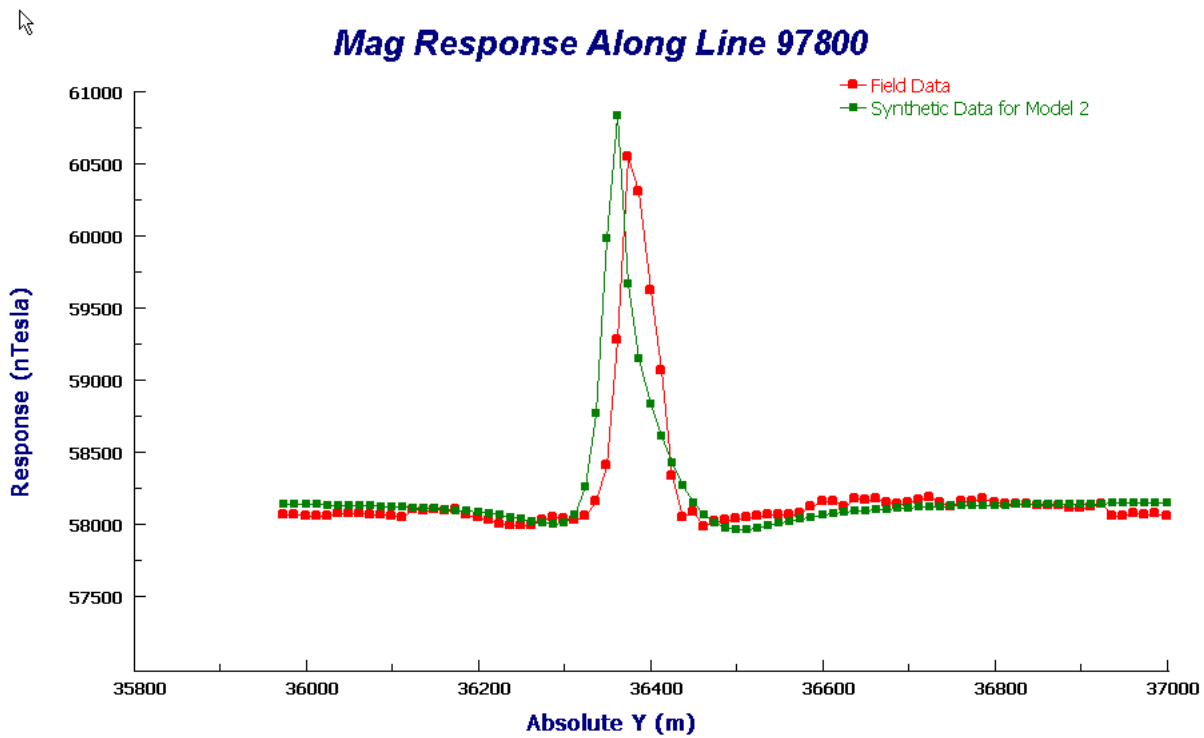


Figure 12a: Comparison of the magnetic response along Line 97800 for the field data and the synthetic data from Model 2.

### Mag Response Along Line 98300

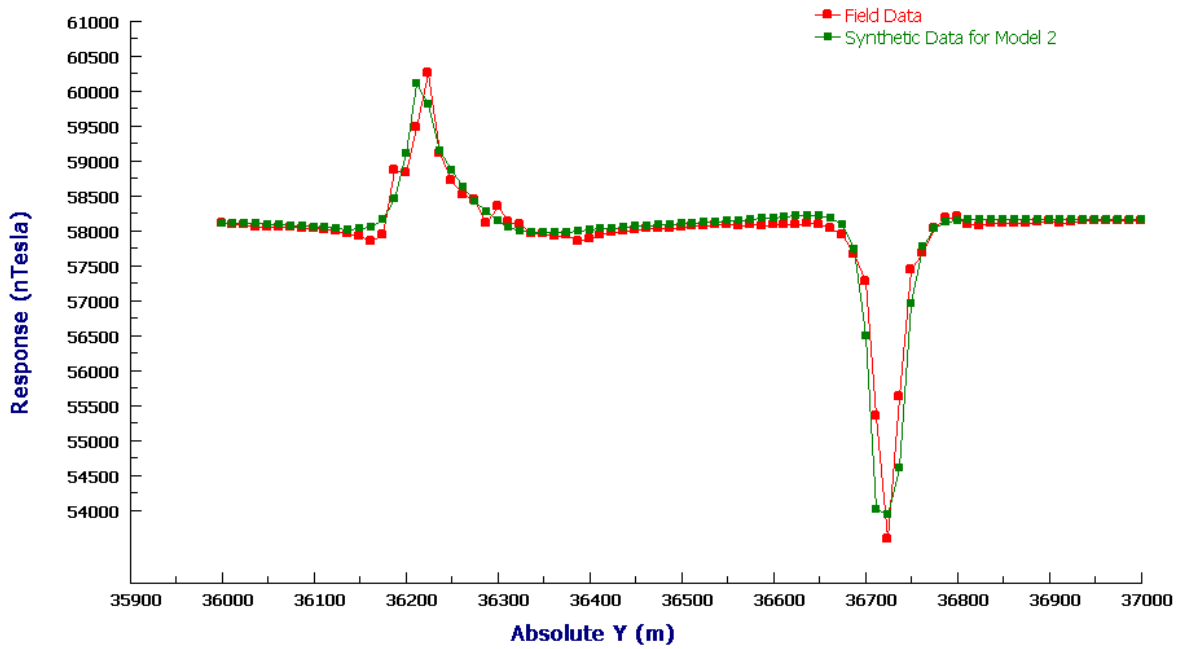


Figure 12b: Comparison of the magnetic response along Line 98300 for the field data and the synthetic data from Model 2.

### Mag Response Along Line 98700

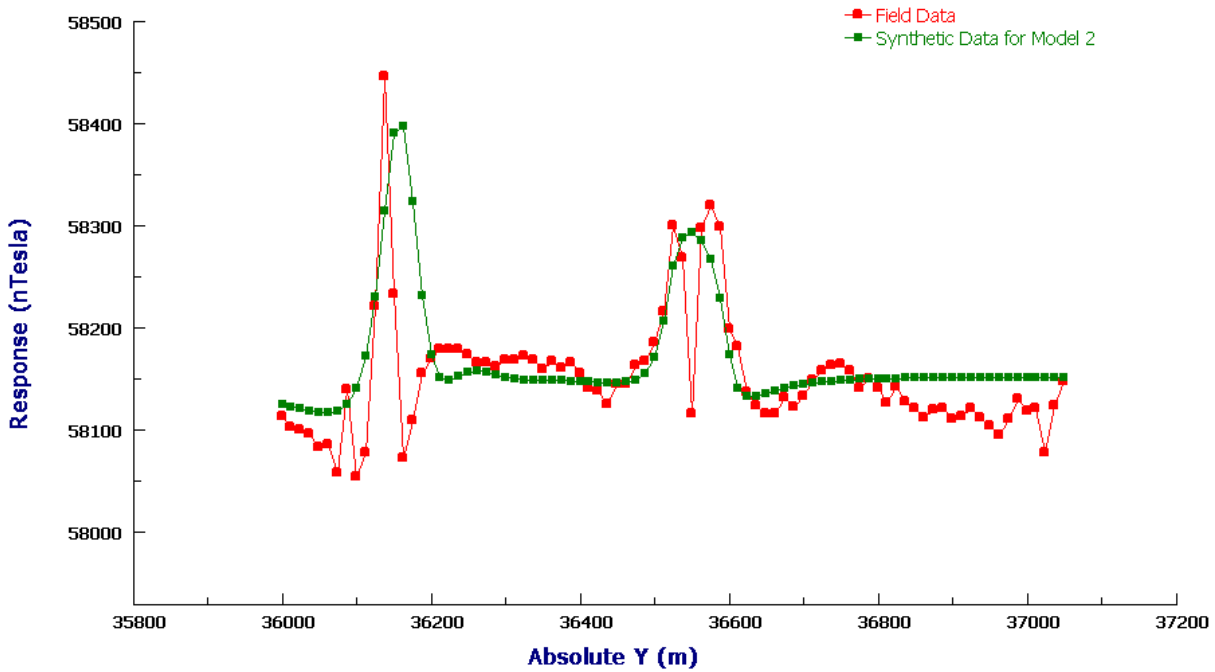


Figure 12c: Comparison of the magnetic response along Line 98700 for the field data and the synthetic data from Model 2.

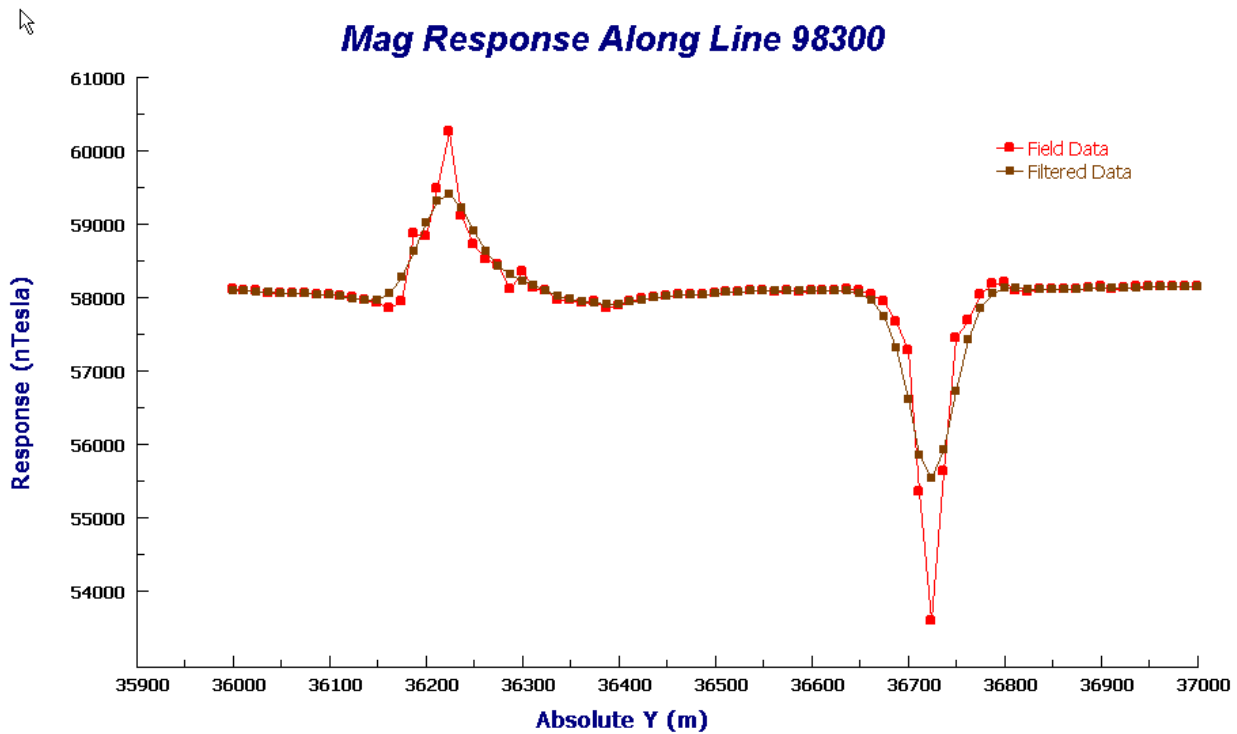


Figure 13: Comparison of the magnetic response along Line 98300 for the field data and the data after 1-D Gaussian filtering. A radius of 74.762 m and a deviation of 18 m were used.

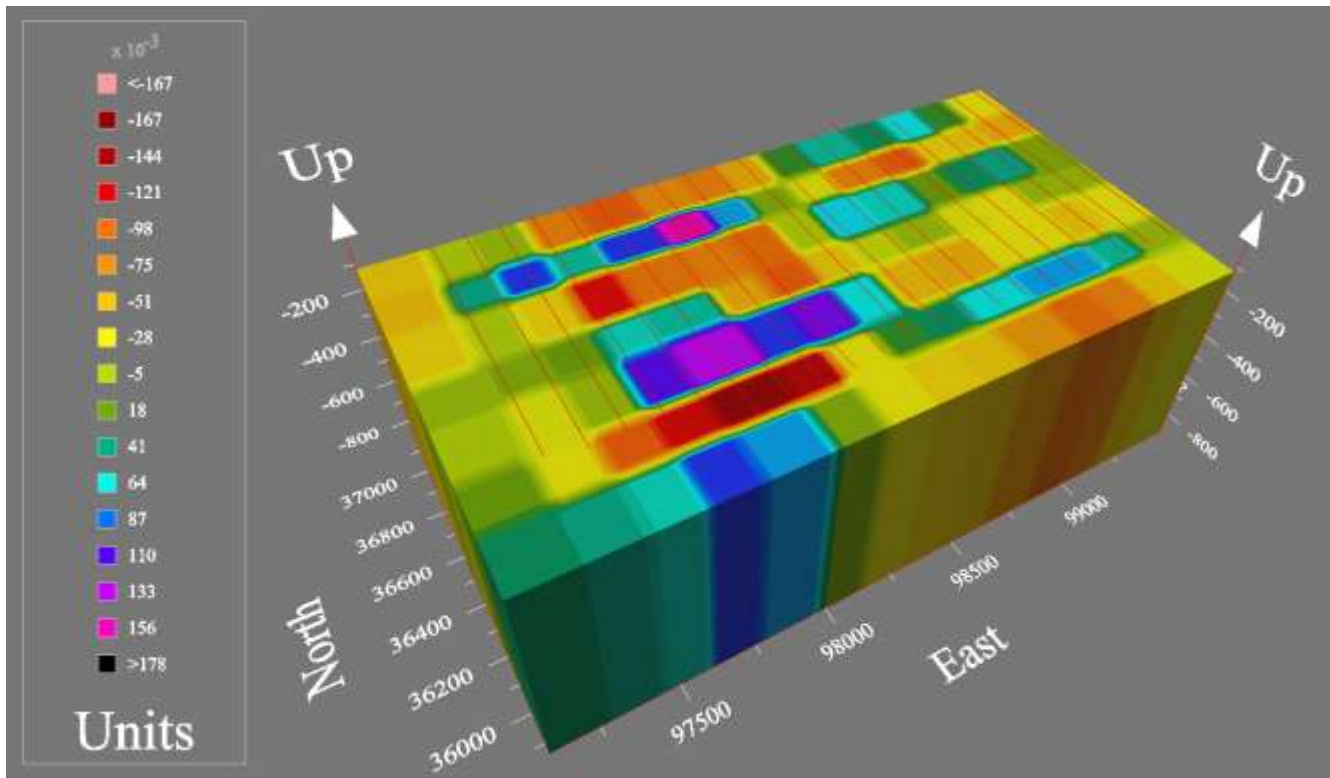


Figure 14: A 3-D contour of the data resulting from a matrix inversion of the field data. The depth of the surface shown is 120 m.

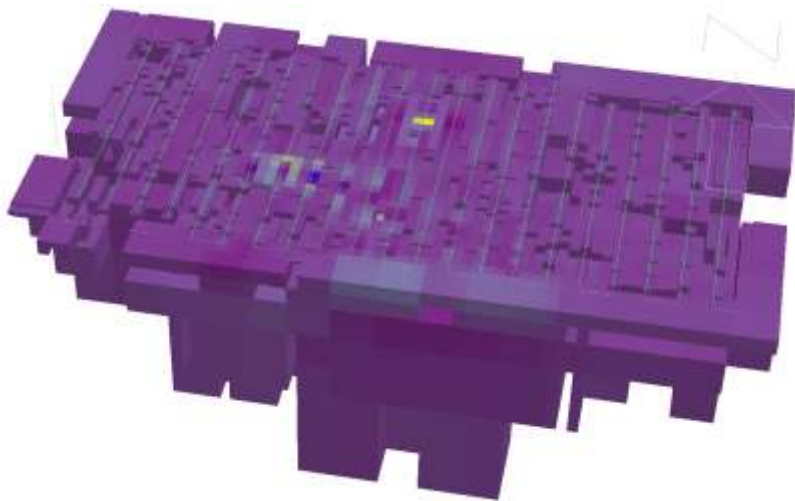


Figure 15a: The model resulting from a fine optimization inversion of the field data, using Model 2 as a starting point.

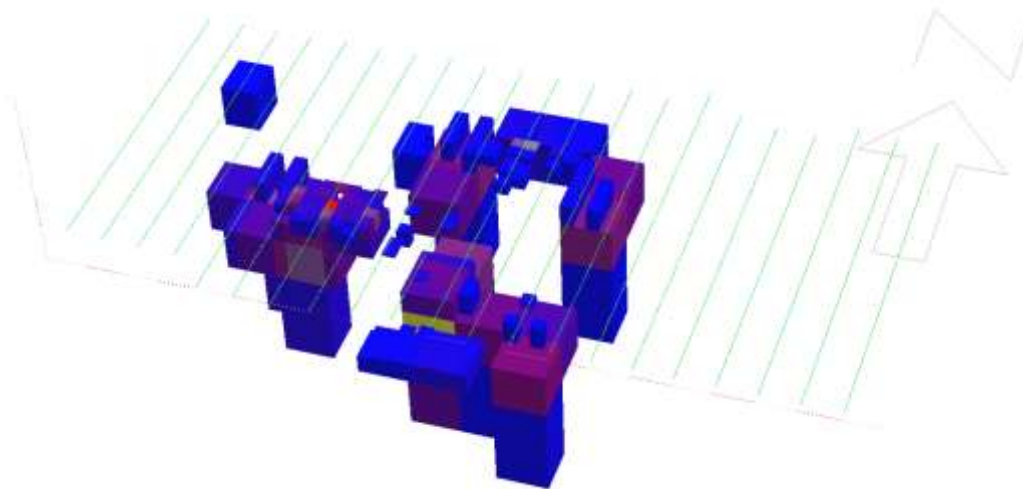


Figure 15b: The model resulting from a fine optimization inversion of the field data, using Model 2 as a starting point. Cells with susceptibilities greater than 0.02 are shown.

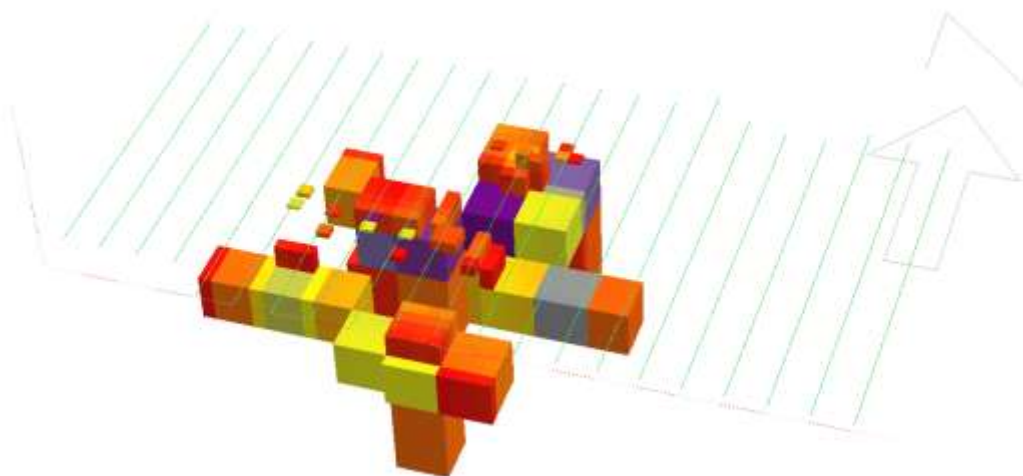


Figure 15c: The model resulting from a fine optimization inversion of the field data, using Model 2 as a starting point. Cells with susceptibilities less than -0.02 are shown.

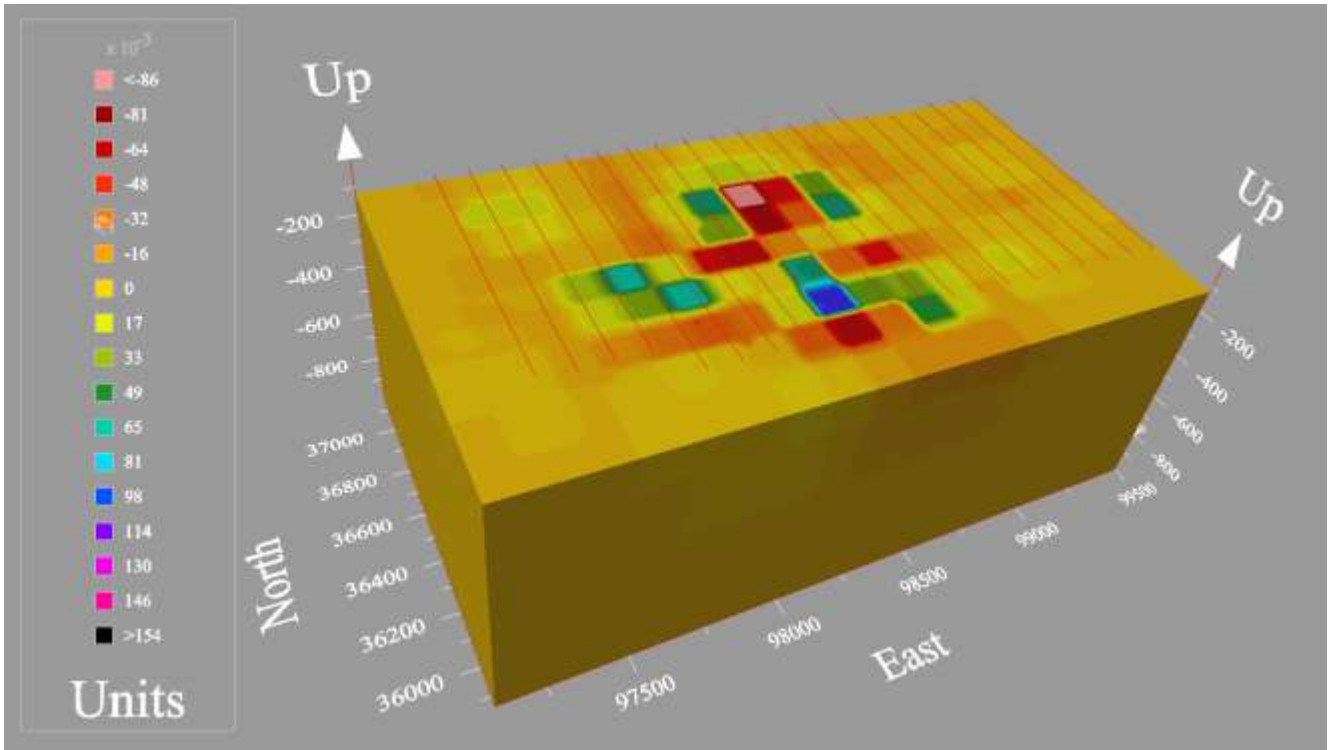


Figure 16: A 3-D contour of the data for Model 15. The depth of the surface shown is 120 m.

### Mag Response Along Line 97800

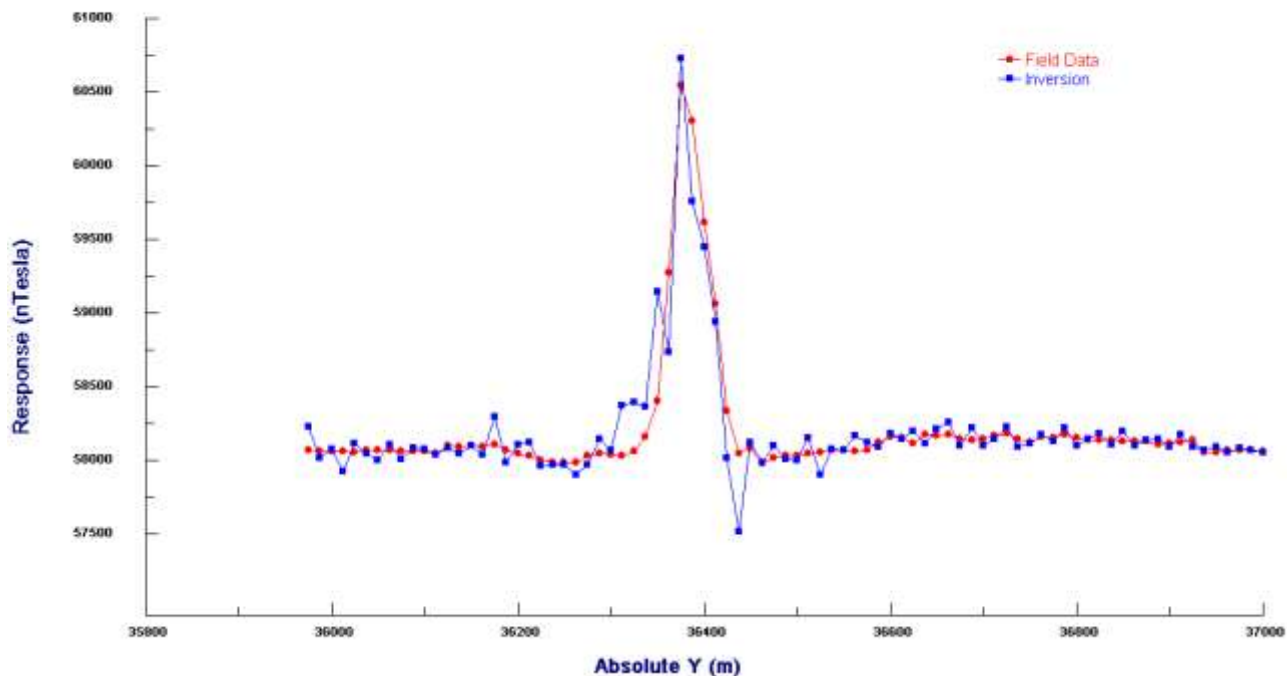


Figure 17a: Comparison of the magnetic response along Line 97 800 for the field data and the synthetic data for the model from the inversion in Figure 15.

### Mag Response Along Line 98300

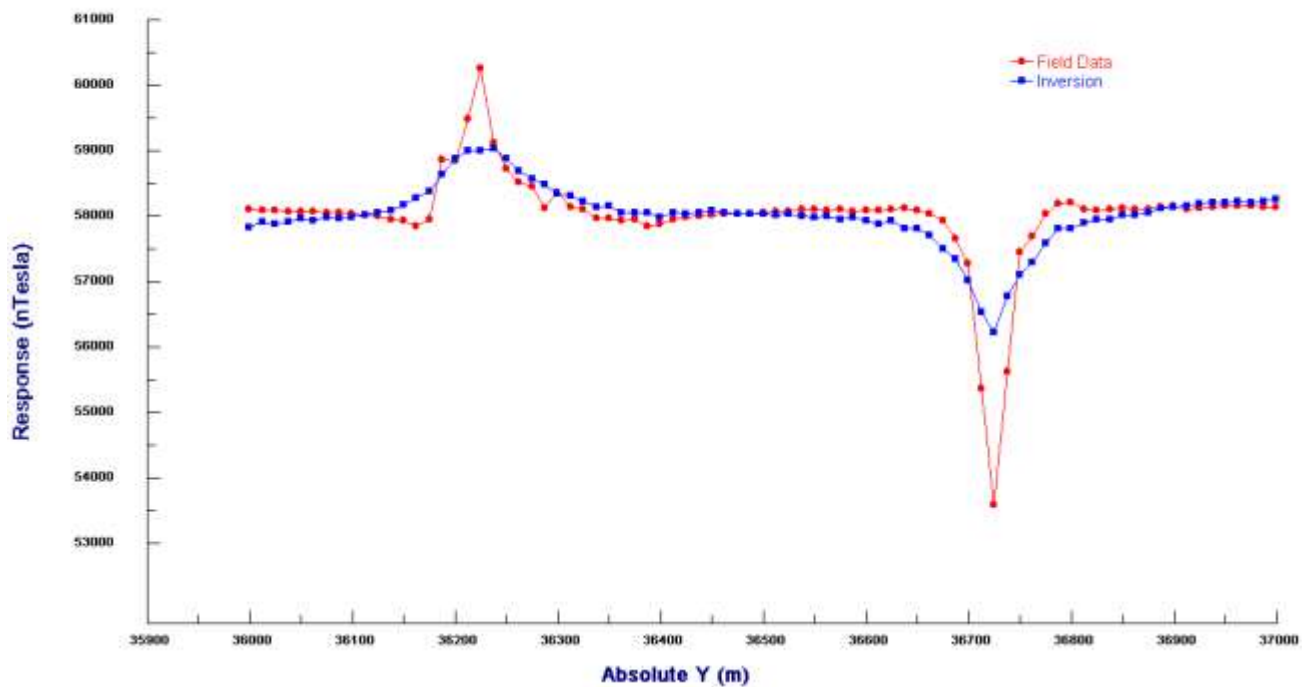


Figure 17b: Comparison of the magnetic response along Line 98300 for the field data and the synthetic data for the model from the inversion in Figure 15.

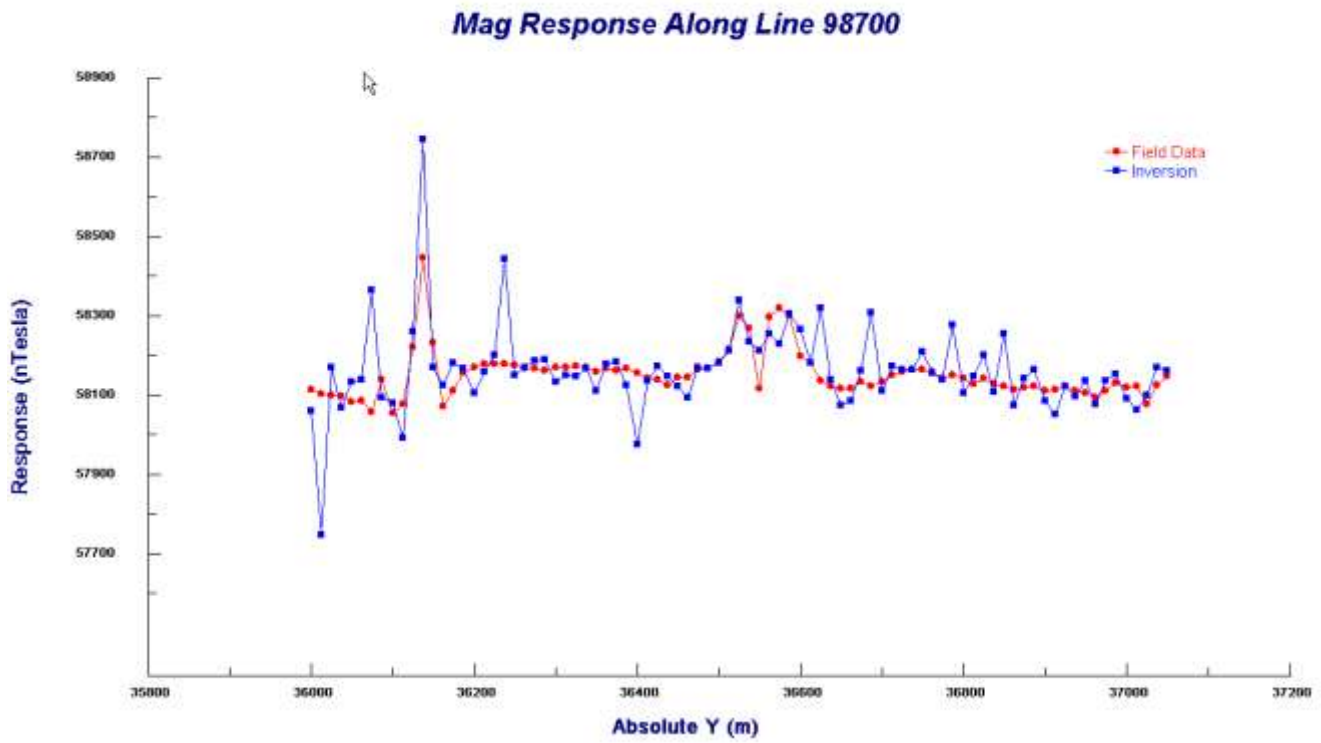


Figure 17c: Comparison of the magnetic response along Line 98700 for the field data and the synthetic data for the model from the inversion in Figure 15.

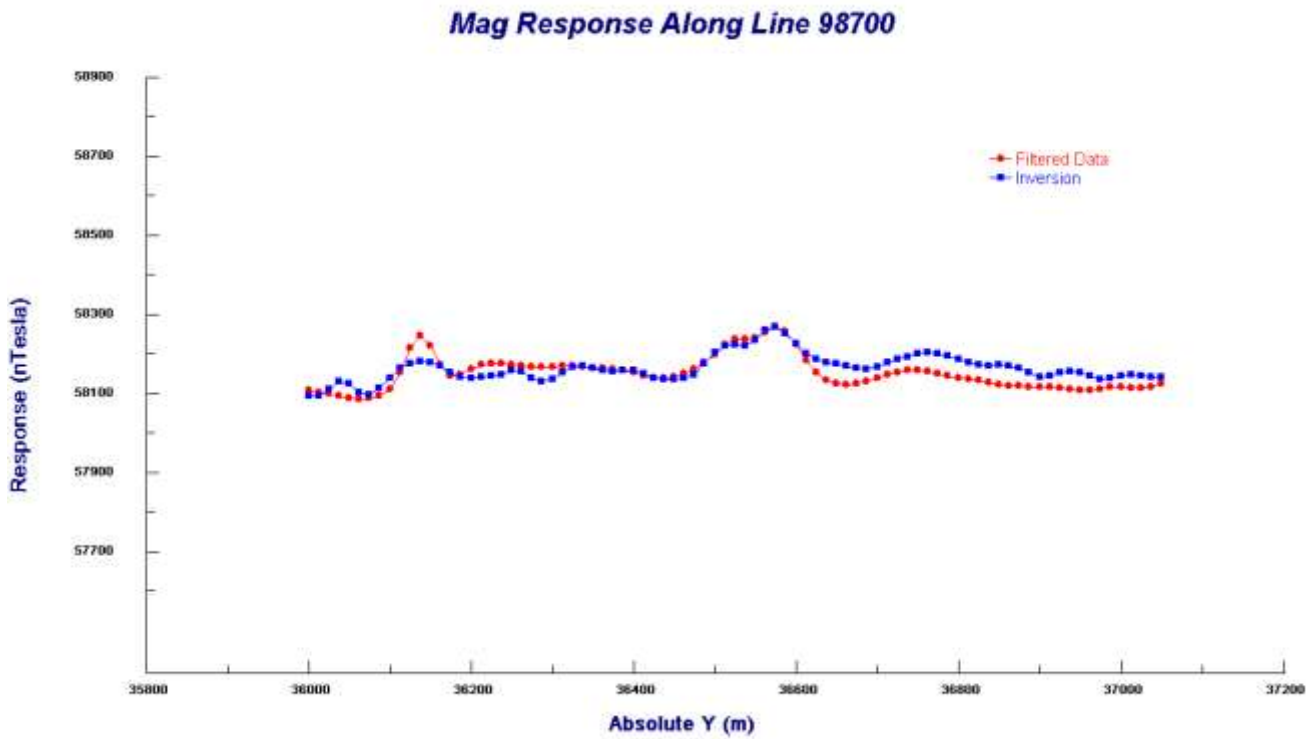


Figure 18: Comparison of magnetic response along Line 98700 for the filtered data and the synthetic data for the model from the inversion of the filtered data.